Research Square

Preprints are preliminary reports that have not undergone peer review.
They should not be considered conclusive, used to inform clinical practice,
or referenced by the media as validated information.

Splice switching of membrane-bound FLT1 into a soluble protein as a treatment for pathological angiogenesis

Layal El Wazan
Centre for Eye Research Australia
Elif Kadife
University of Melbourne
Alesia Harper
University of Melbourne
Satheesh Kumar
Centre for Eye Research Australia
Fiona C Brownfoot
University of Melbourne
Guei-Sheung Liu
rickliu0817@gmail.com

Centre for Eye Research Australia

Article

Keywords: FLT1, VEGF, alternative splicing, splice-switching oligonucleotides, CRISPR activation, retinal vascular disease

Posted Date: November 5th, 2026

DOI: https://doi.org/10.21203/rs.3.rs-11416834/v1

License: This work is licensed under a Creative Commons Attribution 4.0 International License.
Read Full License

Additional Declarations: Competing interest reported. G-S.L. is the Founder and Chief Scientific Officer (CSO) of Adara Bio Pty Ltd. All other authors declare no financial or non-financial competing interests.

Abstract

Pathological retinal neovascularization is associated with dysregulated vascular endothelial growth factor (VEGF) signaling. Soluble FLT1 (sFLT1), an endogenous VEGF decoy receptor, is generated through alternative 3'-end processing of *FLT1* pre-mRNA.

We investigated the cis-regulatory elements that control this process and used splice-switching oligonucleotides (SSOs) to increase sFLT1 production. Two overlapping SSO panels were screened in HEK293FT cells using qPCR and ELISA. We validated lead candidates in CRISPRa-engineered, *FLT1*-enriched Müller glial cells using qPCR, ELISA, and a VEGF-responsive luminescence assay.

Proximal SSOs increased sFLT1 without altering total *FLT1* transcript levels, indicating altered RNA processing rather than increased gene expression. Distal SSOs also enhanced sFLT1 by targeting polyadenylation signals. SSO-16 and SSO-19 produced the greatest increases in sFLT1 and significantly attenuated VEGF signaling.

These findings identify *FLT1* intron 13 regulatory elements as promising therapeutic targets for retinal vascular disease while preserving *FLT1* expression and supporting targeted modulation of VEGF signaling.

Introduction

Vision-threatening retinal vascular diseases, including age-related macular degeneration (AMD) affects over 190 million people worldwide and remain the leading cause of blindness in working-age and older adults [1,2]. Both conditions are driven by pathological neovascularization and vascular leakage due to unregulated vascular endothelial growth factor (VEGF) signaling [3]. Anti-VEGF therapies using exogenous agents have validated suppression of VEGF signaling as an effective therapeutic strategy for retinal vascular disease, substantially improving visual outcomes for millions of patients [4,5]. In contrast, regulation of endogenous anti-VEGF factors has received less attention. One such mechanism operates through alternative splicing of *FLT1*, producing two functionally opposing isoforms: membrane-bound FLT1 (mFLT1), a transmembrane signaling receptor, and soluble FLT1 (sFLT1), a secreted decoy that sequesters VEGF and limits angiogenic signaling [6,7]. Competition between splicing at the exon 13–intron 13 junction and polyadenylation within intron 13 controls the balance between these isoforms. Dysregulated sFLT1 production has been implicated in both retinal vascular disease and preeclampsia [8–10].

Splice-switching oligonucleotides (SSOs) offer a precise approach to modulating the endogenous balance between mFLT1 and sFLT1, and this class of therapeutics has already achieved clinical success in alternative splicing disorders such as Duchenne muscular dystrophy and spinal muscular atrophy [11,12]. Prior work has identified select regulatory elements within *FLT1* intron 13 capable of modulating sFLT1 production, primarily using minigene reporter systems [13]; however, few of the endogenous cis-regulatory sequences governing *FLT1* splice-site selection have been identified, and no retinal cell model

with sufficient endogenous *FLT1* expression has been available to validate candidate SSOs in a disease-relevant context. To address this gap, we systematically screened SSOs spanning the *FLT1* exon 13-intron 13 junction and distal intronic regions in HEK293FT cells, then used CRISPR activation to establish an *FLT1*-enriched Müller glial cell model to validate lead candidates and assess their functional effects on VEGF signaling.

Results

Cis-regulatory elements at the exon 13-intron 13 junction control FLT1 splicing.

To identify cis-regulatory elements involved in alternative *FLT1* splicing, we designed a panel of ten SSOs with 5-nt overlaps spanning the exon 13-intron 13 junction (Fig. 1a). We transfected each SSO individually into HEK293FT cells. We evaluated changes in *FLT1* transcript and protein expression 48 hours later.

PCR and qPCR ($P < 0.0001$) analysis targeting the canonical exon 13–14 splice junction, which is absent from the intron 13-derived soluble *FLT1* isoform, suggested that SSOs targeting sequences immediately upstream of and across the exon 13-intron 13 junction reduced canonical splicing, as represented by SSO-5 to SSO-7 (Fig. 1b and 1c). In contrast, total *FLT1* transcript abundance, quantified using an assay targeting the constitutively expressed exon 8–9 junction present in all mature *FLT1* transcripts, remained unchanged across all treatment groups (Fig. 1d). Together, these findings indicate that SSO treatment at the exon-intron 13 junction altered *FLT1* splice-site selection without affecting overall *FLT1* transcript abundance.

To test whether reduced *mFLT1* transcript level was accompanied by increased sFLT1 production, we quantified secreted protein levels by ELISA. The three SSOs targeting the exon 13-intron 13 junction, SSO-5 to SSO-7, significantly ($P = 0.0003$,

$P < 0.0001$ and $P = 0.0002$, respectively) increased sFLT1 protein secretion compared with the scramble control (Fig. 1e). Notably, two of these oligonucleotides overlapped a previously reported splice-modulating region [9], whereas SSO-5 identified a previously unrecognized regulatory sequence controlling *FLT1* alternative splicing. Interestingly, SSO-9 and SSO-10 increased both *mFLT1* transcript abundance and secreted sFLT1 protein, suggesting that regulatory elements located further within intron 13 may influence *FLT1* processing through mechanisms distinct from disruption of the canonical 5' splice site.

Together, these findings identify multiple proximal cis-regulatory elements that influence *FLT1* splice selection and establish the exon 13-intron 13 junction as a major regulatory region governing endogenous sFLT1 production.

Targeting novel intron 13 cis-elements to promote soluble FLT1 production.

To determine whether distal regions of intron 13 also contribute to *FLT1* splice regulation, a second panel of ten overlapping SSOs was designed approximately 1,968 bp into intron 13, encompassing two intronic polyadenylation sites previously shown by minigene reporter assays to regulate alternative *FLT1* splicing and soluble FLT1 generation [13] (Fig. 2a). Total FLT1 transcript levels remained unchanged across all treatment groups (Fig. 2b), indicating that a targeted block of these regions did not alter overall *FLT1* transcription or regular splice-site usage. Unlike the proximal screen, targeting distal intron 13 produced no detectable changes in *mFLT1* transcript abundance by qPCR (Fig. 2c).

Despite the absence of changes in *mFLT1* expression, ELISA analysis demonstrated significant increases in secreted sFLT1 following treatment with SSO-12 ($P = 0.0045$), SSO-16 ($P = 0.0462$), and SSO-19 ($P = 0.0033$) (Fig. 2d). SSO-12 and SSO-16 overlapped the distal intronic polyadenylation sites previously implicated in sFLT1 generation, whereas SSO-19 identified an additional downstream regulatory region. At the same time, SSO-19 identified an additional downstream regulatory region. These observations differ from earlier minigene studies reporting reduced soluble FLT1 following deletion of distal polyadenylation elements and instead suggest that steric blockade of these endogenous intronic regions enhances sFLT1 production without altering *mFLT1* expression [13].

Collectively, the distal SSO screen identifies a second class of cis-regulatory elements that selectively promote soluble FLT1 production, suggesting that multiple independent regulatory mechanisms cooperate to control FLT1 isoform balance.

CRISPR activation establishes an FLT1-enriched cell model.

The initial SSO screen was carried out in HEK293FT cells owing to their high transfection efficiency. However, their relatively low endogenous *FLT1* expression limited the abundance of *FLT1* splice isoforms available for downstream characterization. As the long-term objective of this work is to develop splice-modulating therapeutics for retinal vascular disease, we sought to establish a more physiologically relevant retinal model with enhanced endogenous *FLT1* expression. To guide the selection of an appropriate retinal cell type, single-cell RNA sequencing data from the adult human retina were examined [14]. *FLT1* expression was enriched in Müller glia compared with most other retinal cell populations. Müller glia also highly expressed *VEGF*, highlighting their central role in retinal angiogenic signaling (Fig. 3a). Based on these expression patterns, we selected the human Müller glial cell line MIO-M1 for subsequent model development.

To increase *FLT1* expression in MIO-M1 cells, we used a plasmid with a U6 promoter driving sgRNA expression and a CMV promoter driving EGFP, T2A, and dCas9-VPR expression. The vector is flanked by 5' and 3' long terminal repeats (LTRs). It includes the woodchuck hepatitis virus post-transcriptional regulatory element (WPRE) to enhance transgene expression (Fig. 3b). To identify an effective CRISPR activation target, five sgRNAs spanning the promoter region of *FLT1* (68–408 bp upstream of the transcriptional start site) were screened in HEK293FT cells (Fig. 3c). Quantitative PCR demonstrated that several sgRNAs increased total *FLT1* transcript expression, with sgRNA4 producing the greatest increase (4.39-fold, $P = 0.0082$) relative to the mock control (Fig. 3d). A similar trend was observed for *FLT1* for the

exon 13–14 junction transcript, where sgRNA4 significantly increased transcript abundance by 4.47-fold ($P = 0.0150$) (Fig. 3e). Consistent with the transcriptional data, ELISA analysis revealed that sgRNA4 also produced the largest increase in secreted sFLT1, reaching approximately 3,700 pg/mL compared with approximately 400 pg/mL in mock-transfected cells ($P < 0.0001$) (Fig. 3f).

Based on these findings, we incorporated sgRNA4 into a lentiviral CRISPR activation system to generate stable cell lines with enhanced endogenous *FLT1* expression. Transduction of HEK293FT cells resulted in an approximately four-fold increase in *FLT1* transcript levels relative to the parental cell line (Fig. 3g). Similarly, transduction of MIO-M1 cells produced a marked increase in endogenous *FLT1* expression by approximately 740-fold relative to the parental cell line (Fig. 3h). Together, these engineered cell lines provide robust models for investigating *FLT1* splice modulation. Given the retinal origin of MIO-M1 cells and their substantially higher endogenous *FLT1* expression after CRISPRa activation, we selected the engineered MIO-M1 cell line for subsequent evaluation of candidate splice-switching oligonucleotides.

Functional sFLT1 produced by SSO treatment suppresses VEGF signaling.

After initial screening in HEK293FT cells, we selected four SSOs for validation in the CRISPRa-engineered MIO-M1 Müller glial cell line. We selected them based on the magnitude of sFLT1 induction observed during the primary screen and to ensure representation of both the proximal and distal splice-regulatory regions identified within intron 13. The selected SSOs comprised SSO-6, which targeted the proximal splice donor region, and SSO-12, SSO-16, and SSO-19, which targeted distal regulatory regions, including the distal polyadenylation sites. Together, these SSOs represented both previously reported and newly identified splice-modulating regions associated with *FLT1* alternative splicing [9,13].

Quantification of total *FLT1* transcripts using a qPCR assay targeting exons 8–9 showed no significant differences between any SSO-treated group and the scramble control (Fig. 4a), indicating that SSO treatment did not alter overall *FLT1* transcription. To further assess the effect of SSO-mediated *FLT1* splicing, we examined two canonical exon junctions associated with the membrane-bound *FLT1* transcript. qPCR analysis of the exon 13–14 junction revealed SSO-specific changes in transcript abundance. SSO-6 significantly reduced the exon 13–14 junction transcript compared with the scramble control ($P < 0.0001$), whereas SSO-12 increased expression ($P = 0.0110$), with SSO-16 and SSO-19 showing no significant changes (Fig. 4b). Analysis of the downstream exon 14–15 junction similarly identified SSO-dependent changes, with SSO-6 reducing expression ($P = 0.0001$) and SSO-12 increasing expression ($P = 0.0004$) relative to the scramble control. In comparison, SSO-16 and SSO-19 did not differ significantly from control (Fig. 4c).

Despite these transcript-level differences, ELISA analysis showed that three of the four SSOs significantly increased sFLT1 secretion. SSO-16 produced the largest mean increase in sFLT1 ($P = 0.0001$), followed by SSO-19 ($P = 0.0006$) and SSO-12 ($P = 0.0013$), whereas SSO-6 induced only a modest, non-significant increase relative to the scramble control (Fig. 4d). These findings indicate that modulation of distinct intronic regulatory regions can promote the production of soluble FLT1 without altering total *FLT1* transcript abundance.

To test whether increased sFLT1 translated into functional inhibition of VEGF signaling, we evaluated conditioned media from SSO-treated MIO-M1 cells using a VEGF-responsive luminescence bioassay. Luminescence values were normalized to cell number to account for differences in cell viability and proliferation between treatment groups. After normalization, conditioned media from SSO-16- and SSO-19-treated cells significantly reduced VEGF signaling compared with the scramble control (P = 0.0413 and 0.0135, respectively), whereas SSO-6 and SSO-12 did not show a significant effect despite increased soluble FLT1 expression (Fig. 4e).

Collectively, these findings show that splice modulation of *FLT1* in Müller glial cells increases production of biologically active sFLT1, which can suppress VEGF signaling. Notably, SSO-16 produced the largest mean increase in sFLT1, whereas SSO-19 produced the strongest reduction in VEGF signaling; these two were not compared directly, and together they identify the distal intronic region as a promising target for RNA-based therapeutic modulation of pathological angiogenesis.

Discussion

Neovascular eye diseases such as AMD and DR remain major causes of vision loss, and while anti-VEGF biologics have transformed clinical management, sustained disease control typically requires repeated intravitreal injection. Endogenous sFLT1 offers an alternative route to the same biological endpoint: rather than introducing an exogenous VEGF-neutralizing agent, SSOs can redirect a cell's own *FLT1* pre-mRNA toward production of this natural VEGF decoy [9]. This study identifies multiple independent cis-regulatory elements in *FLT1* intron 13 that can drive this shift and shows, in a retinal Müller glial cell model, that SSO-induced sFLT1 can reduce VEGF signaling. Together, these findings extend the known regulatory landscape of *FLT1* alternative splicing and identify specific candidate sequences for therapeutic development.

The proximal SSO screen showed that blocking the exon 13-intron 13 splice donor region reduces canonical exon 13–14 splicing while increasing sFLT1 secretion, with no accompanying change in total *FLT1* transcript abundance. This pattern indicates that the SSOs are redirecting post-transcriptional splice-site selection rather than altering overall FLT1 transcription, consistent with SSOs acting on pre-mRNA, since steric-blocking SSOs act on pre-mRNA after transcription has already occurred and would not be expected to influence transcription initiation or total transcript output. SSO-5 identified a regulatory sequence not previously described in the literature, while SSO-6 and SSO-7 overlapped a region reported by Owen and colleagues [9], providing an internal validation of the screening approach. The behavior of SSO-9 and SSO-10 was harder to reconcile with this model, as they increased both *mFLT1* transcript and secreted sFLT1 simultaneously. One possible explanation is that SSO-9 and SSO-10 target a site further from the canonical splice donor that influences splicing efficiency or transcript stability more broadly. Distinguishing between these possibilities will require follow-up experiments, such as single-cell sequencing and isoform screening by mass spectrometry.

The distal SSO screen produced a result that runs counter to prior work using minigene reporter systems, which reported that deletion of distal polyadenylation elements reduces sFLT1 production [13]. In our study, steric blockade of these same regions using SSOs increased sFLT1 secretion without altering *mFLT1* or total *FLT1* transcript levels. This discrepancy may reflect differences between deletion-based and blockade-based splice-manipulation approaches. Removing a polyadenylation element eliminates a cis-regulatory sequence, whereas an SSO occupies that sequence and blocks access by trans-acting factors [15]. It is also possible that minigene constructs lack the native genomic context of the full-length transcript and do not fully capture the transcription-coupled splicing regulation present at the endogenous *FLT1* locus [16]. Because this finding has direct implications for how distal intron 13 is understood to regulate *FLT1* isoform balance, it warrants targeted follow-up, potentially using CLIP-seq to identify the specific proteins engaging this region under each experimental condition [17].

With the ultimate goal of treating pathological retinal angiogenesis, this work aimed to validate the candidate SSOs in retina-relevant cells. Müller glia are a major source of VEGF in the retina and play a central role in both physiological and pathological retinal angiogenesis [18], making them a biologically appropriate target population for this model. Single-cell RNA sequencing data guided the selection of Müller glia as the target population, and CRISPRa-mediated activation of endogenous *FLT1* in the well-characterized human Müller glial line MIO-M1 [19] provided a model with substantially higher *FLT1* expression than unmodified cells, enabling functional assessment of SSO activity. qPCR analysis of the exon 13–14 and exon 14–15 junctions provided additional mechanistic resolution, since both junctions are present only in transcripts that splice canonically through to the mFLT1 reading frame [6]. Their absence defines the intron 13-retained, polyadenylated transcript that gives rise to sFLT1. SSO-6 significantly reduced both junctions, consistent with its position at the proximal splice donor site: by sterically blocking the 3' end of exon 13 immediately upstream of the 5' splice site, SSO-6 appears to force the spliceosome away from the canonical exon 13–14 splicing reaction and toward use of the intronic polyadenylation signal, directly favoring the *sFLT1* transcript at the expense of *mFLT1*. SSO-12, by contrast, significantly increased both junctions, enhancing canonical *mFLT1*-type splicing while also increasing secreted sFLT1 protein (Fig. 4d). This pattern is inconsistent with a simple splice-site competition model. Because total *FLT1* transcript was unchanged (Fig. 4a), this pattern cannot be explained by increased transcription; it is instead consistent with altered processing or stability of specific transcripts, although our data do not resolve the mechanism. Finally, SSO-16 and SSO-19 produced the largest sFLT1 increases and were the only two with a significant functional effect on VEGF signaling, but they produced no significant change at either exon junction. Because canonical splicing was unaffected, the additional sFLT1 in these conditions cannot be explained by diversion away from exon 13–14 splicing. Instead, this pattern points to a mechanism acting downstream of splice-site selection, either by enhanced usage, stability, or processing efficiency of the intron 13 polyadenylation event itself. This distinction between proximal SSO-6 acting through splice-site competition and distal SSO-16 and SSO-19 acting through what appears to be direct modulation of polyadenylation efficiency may also explain why SSO-6's transcript-level effect did not translate into a significant increase in functional sFLT1 protein or VEGF suppression, while SSO-16 and SSO-19's polyadenylation-linked

mechanism did. SSO-16 and SSO-19, which consistently produced the strongest effects across both sFLT1 secretion and VEGF suppression, represent the most promising candidates to advance toward further therapeutic development.

Several features of our model shape how these findings should be interpreted. Because CRISPRa raised endogenous *FLT1* expression about 740-fold in MIO-M1 cells, which was necessary to detect splice isoforms reliably, the regulatory dynamics we observed may differ from those in native Müller glia, and the magnitude of the sFLT1 increases in vivo may be lower. The cell line is also immortalised and may diverge from primary human Müller glia over extended passage [19] and our 2D monolayer culture does not capture the cell–cell signalling or architecture of intact retina. Validation in primary cells, retinal organoids or explants would therefore be a natural next step. The same sequence divergence that limits translation to mouse models also constrains in vivo testing: human and mouse *FLT1* intron 13 share only 73–93% identity across the targeted regions, and in mouse 661W cells a mouse-specific SSO reduced the exon 13–14 junction transcript but SSOs corresponding to the distal polyadenylation sites did not (Supplementary Fig. 1). Delivery, stability and efficacy of these oligonucleotides in retinal tissue have not been tested, and the mechanism underlying the difference between our distal SSO results and earlier minigene findings remains unresolved.

Taken together, our data identify multiple cis-regulatory elements within *FLT1* intron 13 that SSOs can target to increase sFLT1 production, and they show that two distal oligonucleotides, SSO-16 and SSO-19, reduce VEGF signalling in a CRISPRa-engineered Müller glial model. SSO-16 produced the largest mean increase in sFLT1 and SSO-19 the strongest reduction in VEGF signalling, although we did not compare them directly. These two candidates, together with the distal regulatory region they define, are the most promising starting points for in vivo validation in retinal disease models and for dedicated mechanistic studies of how distal intron 13 controls *FLT1* isoform balance.

Methods

Cell Culture

The HEK293FT cell line was purchased from ThermoFisher Scientific (Catalog number R70007). The MIO-M1 cell line was purchased from XIP [19]. Both cell lines were maintained in Dulbecco's Modified Eagle Medium (DMEM) high glucose medium (Gibco, ThermoFisher Scientific, catalog number 11965118) containing 10% fetal bovine serum (FBS) (Gibco, Thermo Fisher Scientific, catalog number: A5670701), 1% GlutaMAX™ Supplement (Gibco, Thermo Fisher Scientific, catalog number: 35050061) and 1% Antibiotic-Antimycotic (100X) (Gibco, Thermo Fisher Scientific, catalog number: 15240062). Cells were grown in a humidified incubator under standard cell culture conditions at 37°C and 5% CO_2.

SSO design

We designed SSOs to block potential splice-modulating regions of the *FLT1* pre-mRNA sterically. The first SSO panel (SSO-1 to SSO-10) spanned the 155 nucleotides at the 3' end of exon 13 and the first 100 nucleotides of intron 13, downstream of an intron 13 in-frame stop codon. Each SSO was 30 nucleotides long and overlapped its neighbor by 5 nucleotides (25-nucleotide step), for a total walk of 255 nucleotides. A second panel (SSO-11 to SSO-20), designed with the same 30-nucleotide, 5-nucleotide-overlap tiling, targeted sequences approximately 1,968 bp from the start of intron 13, encompassing two intronic polyadenylation sites. The scramble control was created by scrambling a randomly selected SSO (https://www.genscript.com/tools/create-scrambled-sequence). To prevent RNase H-mediated cleavage of the target transcript and ensure steric blocking, we synthesized SSOs with a phosphorothioate backbone and 2'-O-methyl RNA bases at all positions using Integrated DNA Technologies. A non-targeting scrambled SSO was used as a negative control. SSO sequences are provided in Supplementary Table 1.

SSO transfection

In a 24-well plate, HEK293FT cells are seeded at a density of 200,000 cells per well. MIO-M1 cells were seeded at 100,000 cells per well in a 12-well plate. 661W cells were seeded at 100,000 cells per well in a 24-well plate. Each SSO was transfected using RNAiMax (ThermoFisher Scientific, Catalog number 13778030) as recommended by the manufacturer. HEK293FT and 661W cells were transfected with a final SSO concentration of 100 nM, 24 hours and 4 hours after seeding, respectively. MIO-M1 cells were transfected with a final concentration of 25 nM SSO, 24 hours after seeding. 48 hours after transfection, we collected cell pellets for RNA analysis and cell culture media for sFLT1 protein analysis.

RNA extraction and cDNA synthesis

RNA was isolated from the HEK293FT and MIO-M1 cells with the Monarch® Total RNA Miniprep Kit (New England Biolabs, Catalog number: T2010S). We inspected RNA quality and quantity using a NanoDrop One Spectrophotometer (ThermoFisher Scientific, catalog number: 840274100). We synthesized cDNA from 200 ng of total RNA using the High-Capacity cDNA Reverse Transcription Kit (ThermoFisher Scientific, catalog number: 4368814).

qPCR design and assay

We used three TaqMan qPCR assays to distinguish changes in overall *FLT1* transcript. The first assay targeted the constitutively expressed exon 8–9 junction, which is present in all known mature *FLT1* transcripts (total *FLT1*), including both membrane-bound and soluble isoforms. The other two assays targeted the exon 13–14 and 14–15 splice junctions, which are generated only when intron 13 is removed through canonical splicing. Because the sFLT1-i13 isoform is produced through intron 13 retention and intronic polyadenylation, transcripts adopting this alternative splicing pathway do not contain the exon 13–14 junction.

The cDNA was diluted (1:10) in nuclease-free water. We performed qPCR using TaqMan™ Fast Advanced Master Mix for qPCR (ThermoFisher Scientific, catalog number: 4444557) in a duplex assay with both the housekeeping and target genes, as per the manufacturer's instructions. We used GAPDH as the internal positive control (IPC). The target gene TaqMan probes used are listed in Supplementary Table 3.

sFLT1 ELISA

Secreted sFLT1 protein levels in conditioned cell culture media were quantified using the Human VEGFR1/Flt-1 DuoSet ELISA (R&D Systems, catalog number: DY321B) according to the manufacturer's instructions. Conditioned media were collected 48 hours after transfection and assayed in duplicate. Absorbance was read at 450 nm using a Tecan Spark plate reader. At the time of media collection, we determined cell number for each well and normalized luminescence values to cell number to account for differences in cell viability and proliferation between treatment groups; we calculated sFLT1 concentrations from a standard curve and normalized them to cell number.

Generation of stable CRISPRa-engineered cell lines

After identifying sgRNA4 (Target sequence: GGCTCGCTTCCCTGCGGCTA) as the lead candidate from the initial screen, we ordered and used a predesigned CRISPRmod CRISPRa All-in-one Lentiviral sgRNA targeting *FLT1* (Horizon Discovery/Dharmacon; catalog number: VSGH12394-251374845) to generate stable CRISPRa-engineered HEK293FT and MIO-M1 cell lines. This all-in-one lentiviral particle co-delivers dCas9-VPR and the sgRNA from a single construct, with a GFP selection marker and CMV promoter. We seeded HEK293FT and MIO-M1 cells at 50,000 cells per well in 24-well plates and incubated them overnight at 37°C. The following day, once cells reached at least 60% confluency, the culture medium was removed and replaced with 1 mL of DMEM containing polybrene (10 µg/mL final concentration, diluted from an 80 mg/mL stock). Lentiviral particles (10 µL per well) were added directly to the polybrene-containing medium, and cells were incubated at 37°C for 72 hours. We then enriched transduced cells successfully by fluorescence-activated cell sorting (FACS) on a BD FACSAria III, gating on EGFP-positive cells.

CRISPRa sgRNA cassette design and cloning

Individual sgRNA-scaffold cassettes (499 bp total, with each sgRNA target sequence contributing 20 nt) were designed using a template vector (Benchling). Candidate p65 activation domain binding sites within the *FLT1* promoter region were predicted using P-Match (gene-regulation.com), and sgRNAs targeting this region for CRISPR activation were designed using CHOPCHOP (chopchop.cbu.uib.no). For each sgRNA, an ampicillin-resistant plasmid backbone (3,378 bp; pUC origin of replication) containing the sgRNA expression cassette — 5' ITR, U6 promoter driving sgRNA expression, sgRNA scaffold, and 3' ITR- was custom-synthesized and cloned by Integrated DNA Technologies (IDT Gene Entry service), as the sequence was not compatible with gBlock synthesis. We received 4 µg of plasmid DNA and diluted it in 20 µL nuclease-free water to a final concentration of 200 ng/µL. We propagated the plasmid by

transforming it into NEB Stable Competent *E. coli* (New England Biolabs, C3040I) according to the manufacturer's protocol. Briefly, we added 1 µL of plasmid DNA (50 ng/µL) to thawed competent cells, incubated them on ice for 30 minutes, heat-shocked them at 42°C for 30 seconds, and returned them to ice. Cells were recovered in 200 µL NEB 10-beta/Stable Outgrowth Medium at 30°C for 60 minutes with shaking, then spread onto carbenicillin selection plates and incubated at 30°C for 24 hours (or 37°C overnight).

Two colonies from each selection plate were picked and grown in 6 mL LB broth containing carbenicillin (1:1000 dilution) overnight at 37°C with shaking at 250 rpm. Plasmid DNA was extracted from each culture using the Monarch® Plasmid Miniprep Kit (New England Biolabs, T1010L), with elution performed in two sequential 30 µL volumes of nuclease-free water (60 µL total per sample), yielding approximately 10 µg of plasmid DNA per sample.

The dCas9-VPR expression plasmid (SP-dCas9-VPR, Addgene plasmid #63798) was recovered from a glycerol stock by streaking onto an LB agar plate. A single colony was picked and grown in 6 mL LB broth containing carbenicillin (1:1000 dilution) overnight at 37°C with shaking. Plasmid DNA was extracted using the Monarch® Plasmid Miniprep Kit (New England Biolabs, T1010L) and eluted in 50 µL elution buffer.

Co-transfection of CRISPRa plasmids for initial sgRNA screening

HEK293FT cells were seeded at 200,000 cells per well in 24-well plates and incubated overnight at 37°C. The next day, cells were co-transfected in duplicate with the dCas9-VPR expression plasmid (11,318 bp) and the corresponding sgRNA expression plasmid (3,251 bp) using Lipofectamine™ 3000 (Thermo Fisher Scientific; catalog number: L3000015), following the manufacturer's protocol. We combined plasmids at a 1:5 VPR:sgRNA molar ratio, corresponding to approximately 7 ng VPR plasmid to 10 ng sgRNA plasmid per fmol; for a total of 500 ng DNA per well, this was approximately 206 ng dCas9-VPR plasmid and 294 ng sgRNA plasmid. The final DNA mixture was gently pipetted before being added dropwise to each well. We collected cell pellets and conditioned media 48 hours post-transfection for RNA extraction and sFLT1 protein analysis, respectively. RNA was extracted using the Monarch® Total RNA Miniprep Kit (New England Biolabs) and reverse-transcribed to cDNA using the High-Capacity cDNA Reverse Transcription Kit (ThermoFisher Scientific), consistent with the RNA extraction and cDNA synthesis methods described above.

VEGF-responsive luminescence bioassay

Functional inhibition of VEGF signaling by SSO-treated conditioned media was assessed using the VEGF Bioassay (Promega, catalog number GA2005), a bioluminescent cell-based assay using KDR/NFAT-RE HEK293 cells engineered to express the NFAT response element upstream of Luc2P together with exogenous KDR (VEGFR2). We tested conditioned media from SSO-transfected CRISPRa-MIO-M1 cells in technical duplicate against a fixed concentration of recombinant VEGF (10 ng/mL) following the

manufacturer's protocol, with a 6-hour incubation before adding Bio-Glo™ Luciferase Assay Reagent. Luminescence was quantified using a Tecan Spark plate reader. At the time of media collection, we determined cell number for each well and normalized luminescence values to cell number to account for differences in cell viability and proliferation between treatment groups. Data are presented from four independent biological replicates.

Single-cell RNA sequencing analysis of the adult human retina

Single-cell RNA sequencing data from the adult human retina were obtained from a previously published dataset generated by our collaborators [14] and provided directly by Prof. Raymond C.B. Wong (Centre for Eye Research Australia, University of Melbourne). We assessed FLT1 and VEGF expression across annotated retinal cell populations, generating dot plots to show the percentage of cells expressing each gene (dot size) and the average normalized expression level per cluster (color intensity).

Use of generative AI

During preparation of this work, the authors used Claude (Anthropic) for language editing and grammar checking. The authors wrote all content. The authors reviewed and edited all text and take full responsibility for the content of the manuscript.

Statistics and reproducibility

Statistical analyses and graphs were generated in GraphPad Prism (version 10.4.2; GraphPad Software). *n* refers to independent biological replicates (separate transfections or transductions performed on separate days), as indicated in each figure legend. Technical replicates (i.e., duplicate wells for ELISA, bioassay and qPCR reactions) were averaged before analysis and were not treated as independent observations. qPCR data were analyzed by the ΔΔCt method, normalized to *GAPDH*, and expressed relative to the scramble SSO, mock-transfected or parental cell control, as stated in each legend. Data are presented as mean ± standard error of the mean (s.e.m.), with individual data points shown. We compared multiple treatment groups against a single control using one-way analysis of variance (ANOVA) followed by Dunnett's multiple-comparisons test, which adjusts for multiple testing; the comparisons of interest were each SSO or sgRNA versus the scramble or mock control. Comparisons between two independent groups used an unpaired, two-tailed Student's *t*-test with Welch's correction where variances were unequal. The significance threshold (α) was 0.05 for all tests. In figures, asterisks denote $P < 0.05$ (*), $P < 0.01$ (**), $P < 0.001$ (***) and $P < 0.0001$ (****).

Declarations

Competing Interests

G-S.L. is the Founder and Chief Scientific Officer (CSO) of Adara Bio Pty Ltd. All other authors declare no financial or non-financial competing interests.

Author Contribution

Conceptualization, L.E.W., G-S.L.; methodology, L.E.W., S.K., G-S.L.; investigation, L.E.W., E.K., A.H., S.K.; writing – original draft, L.E.W., G-S.L.; writing – review & editing, L.E.W., S.K., F.C.B., G-S.L.; funding acquisition, G-S.L.; resources, F.C.B., G-S.L.; supervision, G-S.L. All authors reviewed and approved the manuscript

Acknowledgement

This work was supported by grants from the National Health and Medical Research Council of Australia (NHMRC; GNT1185600) and the CERA Innovation Fund. The funders had no role in study design, data collection, analysis, interpretation, or writing. The John Landman PhD Scholarship supported Layal El Wazan. The Centre for Eye Research Australia receives Operational Infrastructure Support from the Victorian Government. We thank Prof. Raymond C.B. Wong (Centre for Eye Research Australia, University of Melbourne) for generously providing access to the adult human retina single-cell RNA sequencing dataset used in this study. We also thank Dr. Grace Chang for her technical assistance with experiments.

Data Availability

The datasets generated and/or analyzed during the current study are not publicly available due to confidentiality requirements but are available from the corresponding author on reasonable request.

References

1. Wong WL, Su X, Li X, Cheung CMG, Klein R, Cheng C-Y, Wong TY (2014) Global prevalence of age-related macular degeneration and disease burden projection for 2020 and 2040: a systematic review and meta-analysis. Lancet Glob Health 2 (2):e106-116. doi:10.1016/S2214-109X(13)70145-1
2. Zhou J, Chen B (2023) Retinal Cell Damage in Diabetic Retinopathy. Cells 12 (9). doi:10.3390/cells12091342
3. Campochiaro PA (2015) Molecular pathogenesis of retinal and choroidal vascular diseases. Prog Retin Eye Res 49:67-81. doi:10.1016/j.preteyeres.2015.06.002
4. Tah V, Orlans HO, Hyer J, Casswell E, Din N, Sri Shanmuganathan V, Ramskold L, Pasu S (2015) Anti-VEGF Therapy and the Retina: An Update. Journal of Ophthalmology 2015 (1):627674. doi:https://doi.org/10.1155/2015/627674
5. Koksaldi S, Karti O, Saatci AO (2025) Anti-vascular endothelial growth factor therapies in ophthalmology. Med Hypothesis Discov Innov Ophthalmol 14 (3):107-135.

doi:10.51329/mehdiophthal1526

6. Wazan LEI, Widhibrata A, Liu G-S (2024) Soluble FLT-1 in angiogenesis: pathophysiological roles and therapeutic implications. Angiogenesis. doi:10.1007/s10456-024-09942-8
7. Shibuya M (2011) Vascular Endothelial Growth Factor (VEGF) and Its Receptor (VEGFR) Signaling in Angiogenesis:A Crucial Target for Anti- and Pro-Angiogenic Therapies. Genes & Cancer 2 (12):1097-1105. doi:10.1177/1947601911423031
8. Thomas CP, Andrews JI, Liu KZ (2007) Intronic polyadenylation signal sequences and alternate splicing generate human soluble Fltl variants and regulate the abundance of soluble Flt1 in the placenta. The FASEB Journal 21 (14):3885-3895. doi:https://doi.org/10.1096/fj.07-8809com
9. Owen LA, Uehara H, Cahoon J, Huang W, Simonis J, Ambati BK (2012) Morpholino-Mediated Increase in Soluble Flt-1 Expression Results in Decreased Ocular and Tumor Neovascularization. PLOS ONE 7 (3):e33576. doi:10.1371/journal.pone.0033576
10. Maynard SE, Min J-Y, Merchan J, Lim K-H, Li J, Mondal S, Libermann TA, Morgan JP, Sellke FW, Stillman IE, Epstein FH, Sukhatme VP, Karumanchi SA (2003) Excess placental soluble fms-like tyrosine kinase 1 (sFlt1) may contribute to endothelial dysfunction, hypertension, and proteinuria in preeclampsia. The Journal of Clinical Investigation 111 (5):649-658. doi:10.1172/JCI17189
11. Mercuri E, Darras BT, Chiriboga CA, Day JW, Campbell C, Connolly AM, Iannaccone ST, Kirschner J, Kuntz NL, Saito K, Shieh PB, Tulinius M, Mazzone ES, Montes J, Bishop KM, Yang Q, Foster R, Gheuens S, Bennett CF, Farwell W, Schneider E, Vivo DCD, Finkel RS (2018) Nusinersen versus Sham Control in Later-Onset Spinal Muscular Atrophy. New England Journal of Medicine 378 (7):625-635. doi:doi:10.1056/NEJMoa1710504
12. Mendell JR, Rodino-Klapac LR, Sahenk Z, Roush K, Bird L, Lowes LP, Alfano L, Gomez AM, Lewis S, Kota J, Malik V, Shontz K, Walker CM, Flanigan KM, Corridore M, Kean JR, Allen HD, Shilling C, Melia KR, Sazani P, Saoud JB, Kaye EM (2013) Eteplirsen for the treatment of Duchenne muscular dystrophy. Ann Neurol 74 (5):637-647. doi:10.1002/ana.23982
13. Thomas CP, Raikwar NS, Kelley EA, Liu KZ (2010) Alternate processing of Flt1 transcripts is directed by conserved cis-elements within an intronic region of FLT1 that reciprocally regulates splicing and polyadenylation. Nucleic Acids Res 38 (15):5130-5140. doi:10.1093/nar/gkq198
14. Lukowski SW, Lo CY, Sharov AA, Nguyen Q, Fang L, Hung SSC, Zhu L, Zhang T, Grünert U, Nguyen T, Senabouth A, Jabbari JS, Welby E, Sowden JC, Waugh HS, Mackey A, Pollock G, Lamb TD, Wang PY, Hewitt AW, Gillies MC, Powell JE, Wong RCB (2019) A single-cell transcriptome atlas of the adult human retina. The EMBO Journal 38 (18):EMBJ2018100811. doi:10.15252/embj.2018100811
15. Crooke ST, Baker BF, Crooke RM, Liang X-h (2021) Antisense technology: an overview and prospectus. Nature Reviews Drug Discovery 20 (6):427-453. doi:10.1038/s41573-021-00162-z
16. Cooper TA (2005) Use of minigene systems to dissect alternative splicing elements. Methods 37 (4):331-340. doi:https://doi.org/10.1016/j.ymeth.2005.07.015
17. Ule J, Hwang HW, Darnell RB (2018) The Future of Cross-Linking and Immunoprecipitation (CLIP). Cold Spring Harb Perspect Biol 10 (8). doi:10.1101/cshperspect.a032243

18. Li X, Liu J, Hoh J, Liu J (2019) Müller cells in pathological retinal angiogenesis. Transl Res 207:96-106. doi:10.1016/j.trsl.2018.12.006
19. Limb GA, Salt TE, Munro PM, Moss SE, Khaw PT (2002) In vitro characterization of a spontaneously immortalized human Müller cell line (MIO-M1). Invest Ophthalmol Vis Sci 43 (3):864-869

Figures

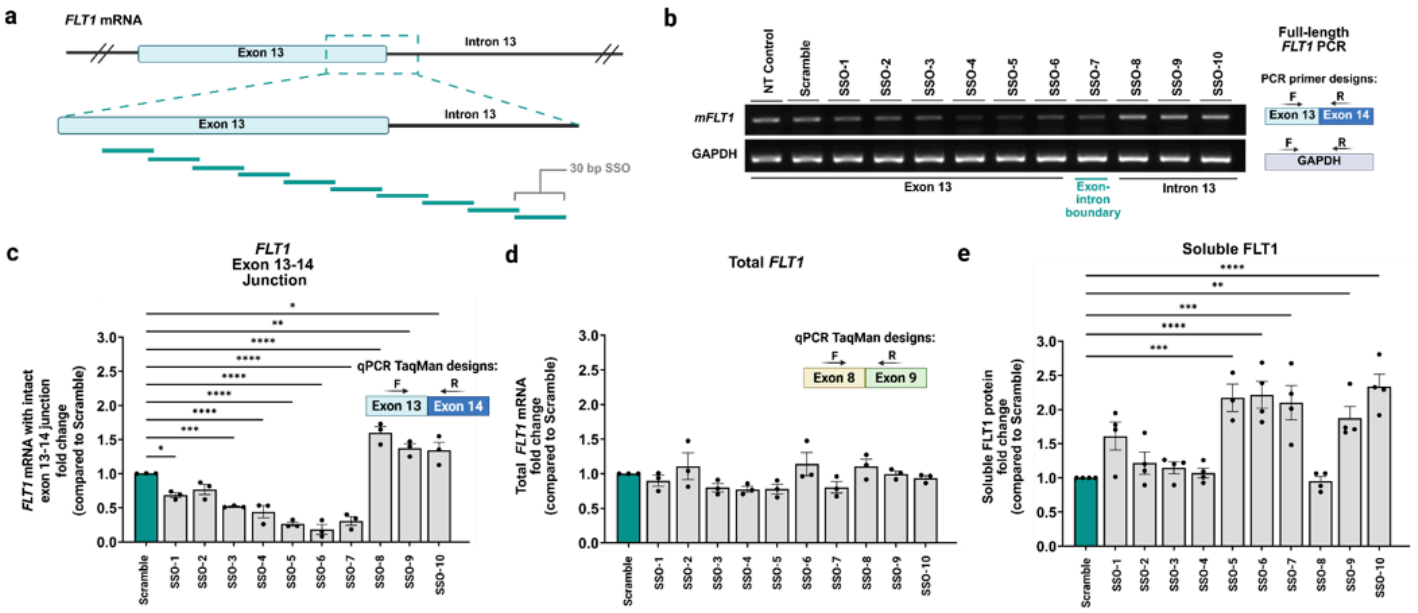


Figure 1

Systematic screening of the exon 13-intron 13 junction identifies cis-regulatory elements that modulate FLT1 alternative splicing. (a) Schematic showing the alignment of the 10 overlapping SSOs targeting the exon 13-intron 13 junction of the human FLT1 transcript. SSO target sequences are provided in Supplementary Table 1. (b) Representative PCR analysis of membrane-bound FLT1 (mFLT1) splice products following SSO transfection in HEK293FT cells (n = 3). PCR primer design is provided in Supplementary Table 2. (c) Quantification of FLT1 transcripts containing the canonical exon 13–14 splice junction by qPCR (n = 3). (d) Quantification of total FLT1 transcript expression by qPCR (n = 3). TaqMan probe information is provided in Supplementary Table 3. (e) Secreted sFLT1 protein levels measured by ELISA 48 h after transfection (n = 4). Gene expression was normalized to GAPDH and is presented relative to the scramble SSO control. Data are presented as mean ± s.e.m. Statistical significance was determined using one-way ANOVA followed by Dunnett's multiple-comparison test. n = independent biological replicates. P < 0.01 (**), P < 0.001 (***), and P < 0.0001 (****). F, forward primer; R, reverse primer. Figure created with BioRender.com.

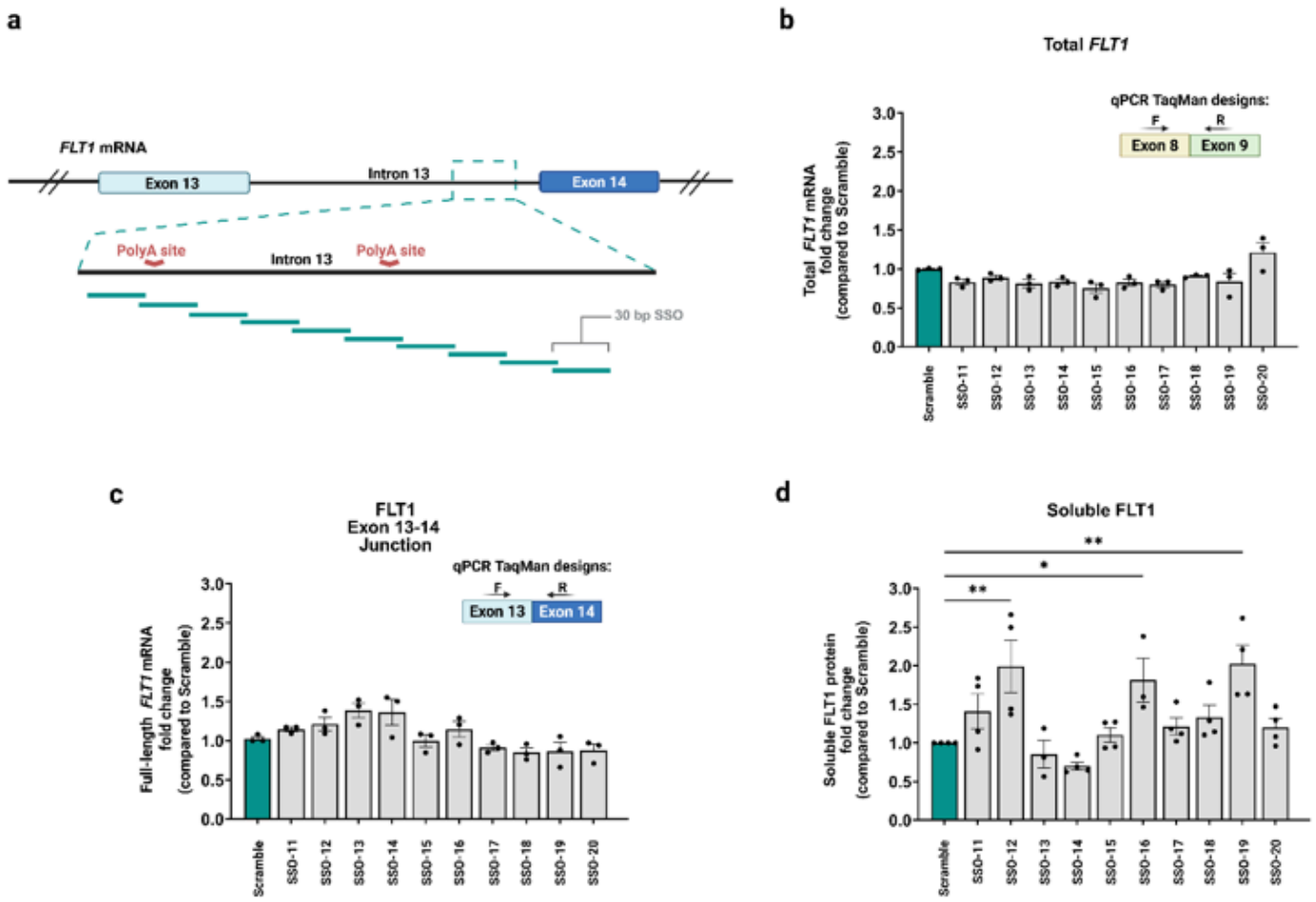


Figure 2

Systematic screening of distal intron 13 SSOs identifies regulatory regions that modulate sFLT1 expression. (a) Schematic showing the alignment of the 10 overlapping SSOs targeting distal regions of intron 13 of the human FLT1 transcript. SSO target sequences are provided in Supplementary Table 1. (b) Quantification of total FLT1 transcript expression by qPCR (n = 3). (c) Quantification of FLT1 transcripts containing the canonical exon 13–14 splice junction by qPCR (n = 3). TaqMan probe information is provided in Supplementary Table 3. (d) Secreted sFLT1 protein levels measured by ELISA 48 h after transfection (n = 4). Gene expression was normalized to GAPDH and is presented relative to the scramble SSO control. Data are presented as mean ± s.e.m. Statistical significance was determined by one-way ANOVA followed by Dunnett's multiple-comparison test. n = independent biological replicates. Significance is indicated as $P < 0.05$ (*), $P < 0.01$ (**). F, forward primer; R, reverse primer. Figure created with BioRender.com.

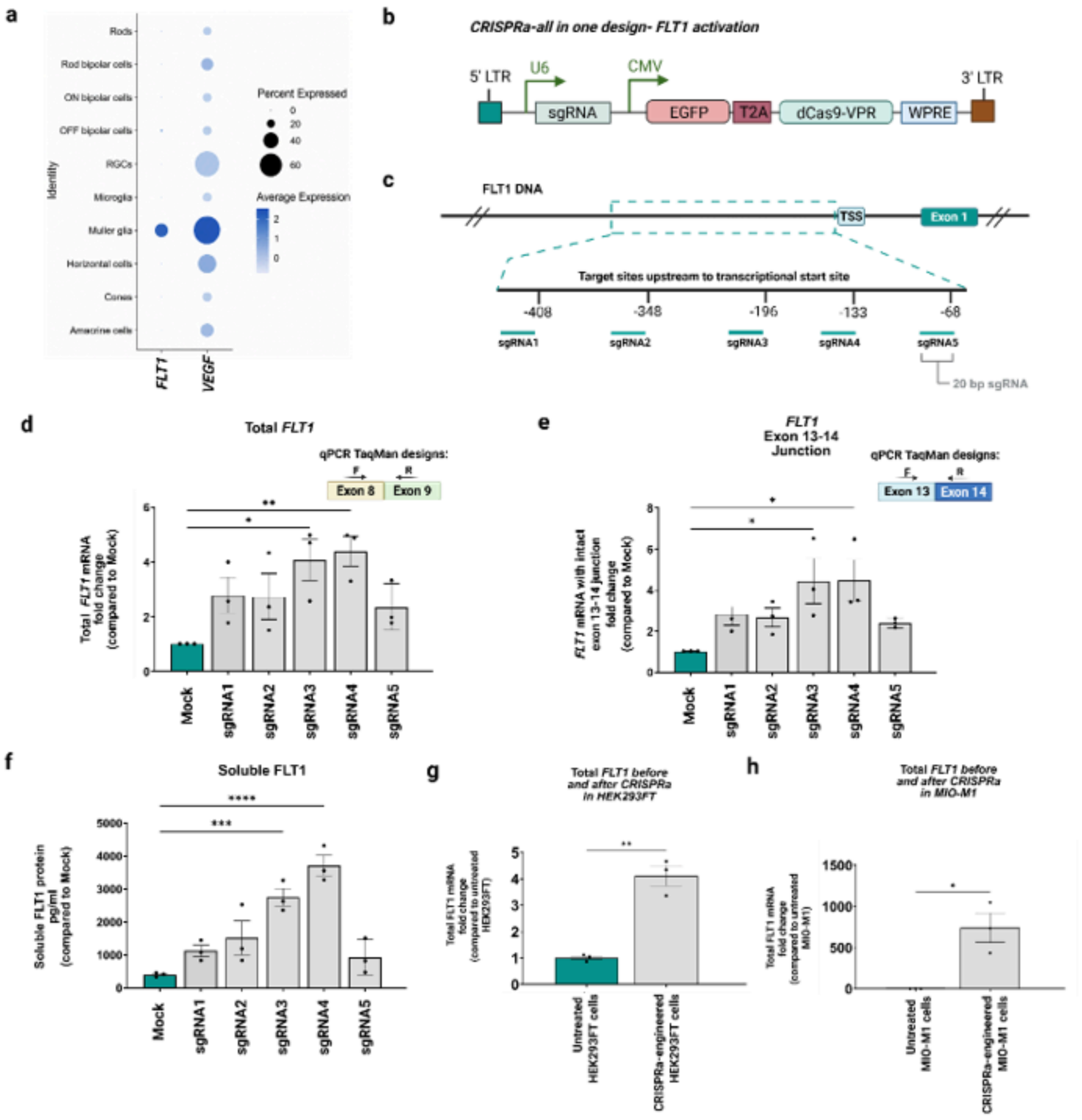


Figure 3

CRISPR activation establishes an FLT1-enriched cell line for downstream splice-modulation studies. (a) Single-cell RNA sequencing analysis of the adult human retina showing the expression of FLT1 and VEGF across major retinal cell populations. Dot size represents the percentage of cells expressing each gene, and color intensity indicates the average normalized gene expression. (b) Schematic of the lentiviral CRISPR activation (CRISPRa) construct used to activate endogenous FLT1 expression. (c) Schematic showing the genomic locations of the five single-guide RNAs (sgRNAs) targeting sequences

upstream of the FLT1 transcriptional start site. sgRNA target sequences are provided in Supplementary Table 4. (d) Quantification of total FLT1 transcript expression by qPCR following transient transfection of each sgRNA in HEK293FT cells (n = 3). (e) Quantification of FLT1 transcripts containing the canonical exon 13–14 splice junction by qPCR (n = 3). TaqMan probe information provided in Supplementary Table 3. (f) Secreted sFLT1 protein levels measured by ELISA 48 h after sgRNA transfection (n = 3). (g) Total FLT1 transcript expression in parental and CRISPRa-engineered HEK293FT cells. (h) Total FLT1 transcript expression in parental and CRISPRa-engineered MIO-M1 cells. Gene expression was normalized to GAPDH and is presented relative to the mock-transfected or parental cell control, as indicated. Data are presented as mean ± s.e.m. Statistical significance was determined using one-way ANOVA followed by Dunnett's multiple-comparison test for panels d-f and an unpaired two-tailed Student's t-test for panels g and h. n = independent biological replicates. Significance is shown as $P < 0.05$ (*), $P < 0.01$ (**), $P < 0.001$ (***), and $P < 0.0001$ (****). F, forward primer; R, reverse primer.Figure created with BioRender.com.

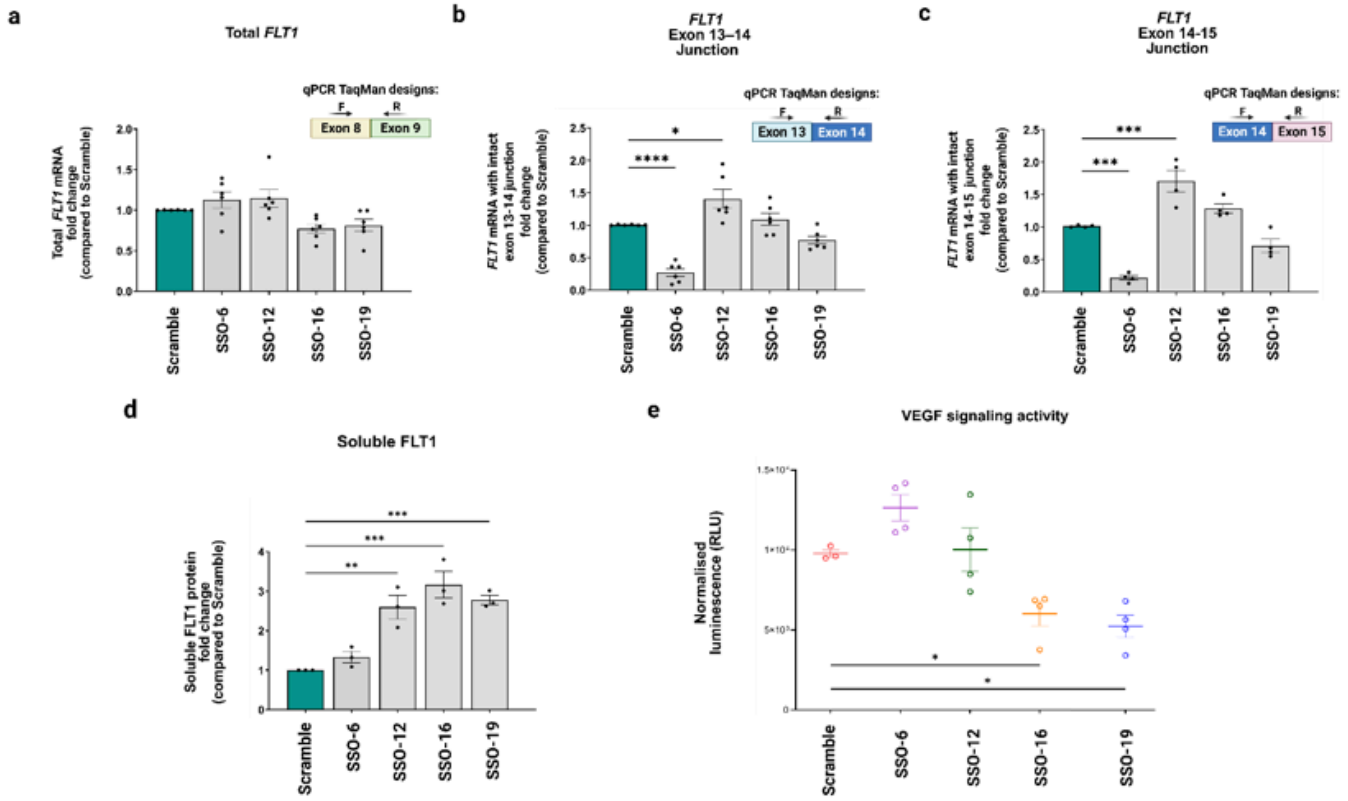


Figure 4

Validation of SSOs in the CRISPRa-engineered MIO-M1 cells. (a) Quantification of total FLT1 transcript expression by qPCR using a TaqMan assay targeting exons 8-9 (n = 6). (b) Quantification of FLT1 transcripts containing the exon 13-14 splice junction by qPCR (n = 6). (c) Quantification of FLT1 transcripts containing the exon 14-15 splice junction by qPCR (n = 4). TaqMan probe information is provided in Supplementary Table 3. (d) Secreted sFLT1 protein levels measured by ELISA 48 h after SSO transfection (n = 3). (e) VEGF signaling activity measured using a VEGF-responsive luminescence

bioassay following treatment with conditioned media collected from SSO-transfected cells (n = 4). Luminescence values were normalized to cell number, with reduced luminescence indicating greater inhibition of VEGF signaling. Gene expression was normalized to GAPDH and is presented relative to the scramble SSO control. Data are presented as mean ± s.e.m. Statistical significance was determined using one-way ANOVA followed by Dunnett's multiple-comparison test. n = independent biological replicates. Significance is shown as $P < 0.05$ (*), $P < 0.01$ (**), $P < 0.001$ (***), and $P < 0.0001$ (****). F, forward primer; R, reverse primer. Figure created with BioRender.com

Supplementary Files

This is a list of supplementary files associated with this preprint. Click to download.

- WazanEletalsFLTSSOSupplementary.docx
- SupplementaryFigure1.png